



1 **Physical processes influencing the Asian climate due to black carbon emission**
2 **over East and South Asia**

3 *Feifei Luo¹, Bjørn H. Samset², Camilla W. Stjern², Manoj Joshi³, Laura J. Wilcox⁴,*
4 *Robert J. Allen⁵, Wei Hua¹, and Shuanglin Li^{6,7}*

5 1. School of Atmospheric Sciences/Plateau Atmosphere and Environment Key
6 Laboratory of Sichuan Province/Meteorological Disaster Prediction and Warning
7 Engineering Laboratory of Sichuan Province, Chengdu University of Information
8 Technology, Chengdu, China

9 2. CICERO Center for International Climate Research, Oslo, Norway

10 3. Climatic Research Unit, School of Environmental Sciences, University of East
11 Anglia, Norwich, United Kingdom

12 4. National Centre for Atmospheric Science, University of Reading, Reading, United
13 Kingdom

14 5. Department of Earth and Planetary Sciences, University of California Riverside,
15 Riverside, CA, United States of America

16 6. Climate Change Research Center, Institute of Atmospheric Physics, Chinese
17 Academy of Sciences, Beijing, China

18 7. Department of Atmospheric Science, China University of Geoscience, Wuhan,
19 China

20 Corresponding author: Feifei Luo (lff@cuit.edu.cn)

21



23

Abstract

24 Many studies have shown that black carbon (BC) aerosols over Asia have
25 significant impacts on regional climate, but with large diversities in intensity, spatial
26 distribution and physical mechanism of regional responses. In this study, we utilized a
27 set of Systematic Regional Aerosol Perturbations (SyRAP) using a reduced complexity
28 climate model, FORTE2, to investigate responses of the Asian climate to BC aerosols
29 over East Asia only, South Asia only, and both regions at once, and thoroughly examine
30 related physical processes. Results show that regional BC aerosols lead to a strong
31 surface cooling, air temperature warming in the low-level troposphere, and drying over
32 the perturbed areas, with seasonal differences in magnitude and spatial distribution.
33 Atmospheric energy budget analysis suggests that reductions in local precipitation
34 primarily depend on the substantial local atmospheric heating due to shortwave
35 absorption by BC. Increases in dry static energy (DSE) flux divergence partly offset the
36 reduced precipitation over north China in summer and most of China and India in the
37 other three seasons. Decreases in DSE flux divergence lead to stronger reduction in
38 precipitation over south China and central India in summer. Changes in DSE flux
39 divergence are mainly due to vertical motions driven by diabatic heating in the middle
40 and lower troposphere. BC perturbations also exert non-local climate impacts through
41 the changes in DSE flux divergence. This study provides a full chain of physical
42 processes of the local climate responses to the Asian BC increases, and gives some
43 insights to better understand the uncertainties of model responses.

44



45 1. Introduction

46 Black carbon (BC) aerosol, a short-lived pollutant and climate forcer, is emitted
47 from the incomplete combustion of biomass and fossil fuels, and exerts significant
48 effects on global and regional climate (Ramanathan and Carmichael, 2008; Bond et al.,
49 2013; Stjern et al., 2017; IPCC, 2021; Li et al., 2022). Alongside rapid economic
50 developments of China and India over the past few decades, East and South Asia have
51 become the highest BC emissions hotspots in the world. Despite BC emissions from
52 China decreasing substantially in the past decade, East and South Asia are expected to
53 remain the highest BC loadings globally in the coming decades (Lund et al., 2019).
54 Hence, the climate impacts of BC emissions from East and South Asia have been
55 extensively investigated (e.g. Li et al., 2016; Lou et al., 2019; Xie et al., 2020;
56 Westervelt et al., 2020; Herbert et al., 2022; Yang et al., 2022). Although many model
57 studies have shown that Asian BC aerosols are of great importance for local climate
58 (especially the Asian monsoonal systems), considerable uncertainty exists regarding the
59 intensity and spatial distribution of the Asian climate responses to BC forcings, as well
60 as the related physical mechanisms.

61 Menon et al. (2002) found that during summer, a large BC forcing induced a
62 “southern flooding and northern drought” (SFND) precipitation pattern in China, and
63 moderate cooling in China and India based on the Goddard Institute for Space Studies
64 (GISS) global climate model (CGCM). However, many subsequent studies were not
65 able to reproduce the SFND pattern, in part due to the poor representation of the Asian
66 summer monsoon in models (Wilcox et al., 2015). Gu et al. (2006) found that BC
67 forcing acted to suppress precipitation in southern and eastern China due to warming in
68 the middle to high latitudes based on an atmospheric general circulation model
69 (AGCM). Zhang et al. (2009) showed that the effects of direct radiative forcing due to
70 increased BC aerosols can decrease precipitation and increase surface temperature in
71 southern China and India, but cause the opposite responses in northern China, by
72 comparing CAM3 AGCM simulations with the all-aerosol types and without
73 carbonaceous aerosol. Liu et al. (2018) found a similar dipole precipitation pattern with
74 a decrease in southern China and an increase in the north mainly due to the fast



75 adjustments (simulations with fixed SST) of BC forcing, and a surface cooling over
 76 Asia except over the Himalayan region in the 10x modern Asian BC emissions or
 77 concentrations experiments in the Precipitation Driver Response Model
 78 Intercomparison Project (PDRMIP) (Myhre et al., 2017).

79 Wang et al. (2017) conducted CESM1 simulations with increased BC emissions
 80 from preindustrial to present-day level, and proposed that the fast adjustment
 81 strengthened the EASM, while slow adjustment (response to aerosol-induced SST
 82 change) dominated the spatial pattern of precipitation response, which showed a tripolar
 83 precipitation pattern with wetting-drying-wetting from north to south China, although
 84 the responses in most regions were statistically insignificant. The fast/slow responses
 85 in Wang et al. (2017) are different with those in Liu et al. (2018). Xie et al. (2020) used
 86 the PDRMIP ensemble to show that the extremely high global/Asian BC forcing can
 87 cause the similar tripolar precipitation pattern over eastern China in summer, and they
 88 stressed that these responses mainly result from the enhanced upper-level atmospheric
 89 temperature over Asia instead of low-level thermal feedbacks. Mahmood and Li (2014)
 90 showed that South Asian BC also can induce the tripolar precipitation pattern over East
 91 China via a propagating wave train along the Asian upper tropospheric jet based on
 92 ensemble sensitive experiments in GFDL AM2.1.

93 Persad et al. (2017), based on GFDL AM3, have shown that surface solar dimming
 94 dominates the reduction of the East Asian summer precipitation due to the decreased
 95 land-sea contrast, whilst atmospheric heating from absorbing aerosols partially offset
 96 the reduction, which leads to a smaller reduction when both effects are considered
 97 simultaneously. Jiang et al. (2013) and Guo et al. (2013) indicated that there was no
 98 statistically significant change in precipitation over East China in response to global
 99 BC forcing during summertime, based on the CAM5 and HiGAM AGCM experiments,
 100 respectively. Although there are many differences across studies, some similarities can
 101 still be found in most of studies, such as surface cooling in the perturbation area, wet
 102 response in North China.

103 In addition, some AGCM/CGCM studies suggested that increased BC aerosols can
 104 lead to a weakened South Asian summer monsoon (SASM) (Lau and Kim, 2007; Meehl



105 et al., 2008), while others found that there should be a strengthened SASM via
 106 increasing the atmospheric meridional land-sea thermal gradient, or an elevated heat
 107 pump effect (Lau and Kim et al., 2006; Xie et al., 2020; Westervelt et al., 2020). On the
 108 other hand, Westervelt et al. (2018) conducted aerosol removal experiments using three
 109 CGCMs, and found that Indian BC decreases lead to no change or a small decrease in
 110 precipitation in India.

111 By comparing the sum of Asian summer climate responses to individual responses
 112 over East and South Asia with the responses to simultaneous forcing, the regional
 113 linearity of BC forcing has been investigated. Chen et al. (2020) and Herbert et al. (2022)
 114 suggested that the responses were highly nonlinear due to the interaction of atmospheric
 115 circulation changes, based on the regional climate model RegCM4 and the Intermediate
 116 General Circulation Model 4 (IGCM4) simulations, respectively. In contrast, Reccia
 117 and Lucarini (2023) and Stjern et al. (2024) found that the responses were almost linear
 118 in most of Asian regions. The difference may be related to the different spatial extend
 119 of the aerosol perturbation in the simulation design (Stjern et al., 2024).

120 For the East Asian winter climate, Jiang et al. (2017) found that BC forcing can
 121 lead to an intensification of the East Asian winter monsoon (EAWM) northern mode
 122 via heating Tibetan Plateau using the CAM5 model. On the contrary, Lou et al. (2019)
 123 suggested that BC emitted from the North China can weaken the EAWM through ocean,
 124 sea ice, cloud feedbacks based on CESM. BC aerosol also can impact on spring and
 125 autumn precipitation in China (Guo et al., 2013; Hu and Liu et al., 2014; Deng et al.,
 126 2014).

127 These inconsistent results, and the large uncertainty in the simulated response of
 128 the Asian climate to BC changes, are partly related to differences in the modeling
 129 approach (e.g., AGCMs versus CGCMs/ESMs) and also the magnitude and location of
 130 the BC perturbation. Atmosphere-only GCMs lack SST feedbacks, which are crucial in
 131 influencing the Asian monsoon (Dong et al., 2019), while CGCMs or ESMs involving
 132 more and complex physical processes make it difficult to identify the key physical
 133 processes of impacts of regional BC aerosols on Asian climate. The inconsistency may
 134 also be associated with model-specific differences. Different models that include



different physical processes, combined with different experiment designs that can influence the atmospheric circulation response, mean that understanding the causes of differences between studies is very difficult. Hence, reduced complexity models, such as FORTE2 (Fast Ocean Rapid Troposphere Experiment version 2), provide an alternative and useful tool for such studies, given that such models not only include all the main mechanisms of aerosol-climate interactions, but also allow fast speed of integration and longer simulations with lower cost. Stjern et al. (2024) have utilized FORTE2 to perform a series of Systematic Regional Aerosol Perturbations (SyRAP) simulations with absorbing and scattering aerosol species in East Asia only, South Asia only, and both regions simultaneously. Their results have shown that SyRAP-FORTE2 is a helpful framework to understand and decompose the local and remote climate effects of regional aerosol emissions.

Therefore, based on the simulations of the regional BC perturbations in SyRAP-FORTE2, this study aims to address the following two questions: (1) what are responses of Asian climate to either East Asian or South Asian BC emissions, or both regions at once, respectively? (2) What are key physical processes involved in these responses?

The rest of the paper is organized as follows: section 2 describes the FORTE2 model, the SyRAP simulations, and the analysis methods and datasets; section 3 briefly evaluates the climatology of SyRAP simulations, examines responses to the regional BC perturbations in SyRAP-FORTE2, and investigates the underlying physical processes involved in these responses; section 4 compares the results of the atmospheric energy budget in SyRAP-FORTE2 with those in the PDRMIP models; Finally, the summary and discussion are provided in section 5.

2. Methods

2.1 The FORTE2 model

FORTE2 is an intermediate-complexity coupled atmosphere-ocean general circulation model (Blaker et al., 2021). The atmospheric component is the Intermediate General Circulation Model 4 (IGCM4) with a horizontal resolution of approximately 2.8° (T42), and 35 sigma levels extending up to 0.1 hPa (Joshi et al., 2015). IGCM4



164 includes schemes for radiation, land-surface properties, convection, precipitation, and
165 clouds (Zhong and Haigh, 1995; Betts and Miller, 1993). The oceanic component is the
166 Modular Ocean Model-Array (MOMA) with a horizontal grid spacing $2^\circ \times 2^\circ$, and 15 z-
167 layer levels increasing in thickness with depth from 30m at the surface to 800m at the
168 bottom (Webb, 1996). Sea ice is represented by a barrier to heat fluxes between the
169 ocean and atmosphere components. FORTE2 runs without flux adjustments (Blaker et
170 al., 2021). Blaker et al. (2021) have thoroughly evaluated the skill of FORTE2 in
171 simulating the atmosphere, ocean and major climatic modes. Hence, given the
172 advantages of FORTE2 in terms of running speed, flexibility and economy, it is a useful
173 tool to study a wide range of climate questions. For the SyRAP-FORTE2 simulations,
174 FORTE2 was updated to include a parameterization of aerosol-cloud interactions,
175 where cloud droplet effective radius in low- and mid-level clouds is reduced from $15\mu\text{m}$
176 to $10\mu\text{m}$ in regions where optical depth is greater than 0.07. However, this
177 parameterization is only applied for scattering aerosol, and is not used in the BC
178 experiments described in the following section. The semi-direct effect of BC is included.

179 2.2 The SyRAP-FORTE2 simulations

180 Stjern et al. (2024) performed a set of SyRAP experiments using the FORTE2
181 model. The main simulations include: (1) baseline simulations forced by GHG
182 concentrations at different climate states (i.e. preindustrial, present-day and future CO_2
183 levels) and no aerosol; (2) perturbation simulations forced by added absorbing (BC, and
184 organic carbon, OC) or scattering (sulfate, SO_4) aerosols over East Asia only, South
185 Asia only, and over both regions simultaneously with only aerosol-radiation
186 interactions (ARI), and GHG concentrations at different climate states; (3) Aerosol-
187 cloud interactions (ACI) simulations forced by added SO_4 in the combined East Asia
188 and South Asia region in which the ACI were turned on. This study focusses on the
189 effects of adding regional BC perturbations, but the SyRAP-FORTE2 design allows the
190 impacts of different aerosol species to be compared in a consistent framework.

191 FORTE2 did not use aerosol gas emissions/concentrations as most CMIP6 models
192 use. Instead, the global gridded monthly aerosol optical depths (AOD) and vertical



193 distributions were used from the Copernicus Atmosphere Monitoring Service reanalysis
 194 (CAMSRA) during 2003-2021 (Inness et al., 2019). Aerosols are not transported in
 195 FORTE2. The application of aerosol distributions from a reanalysis means that the
 196 simulations include a realistic aerosol spatial distribution, but the lack of aerosol
 197 transport means that there are no feedbacks between the climate response and the
 198 aerosol distribution (e.g. increased precipitation leading to increased aerosol removal).
 199 All simulations were run for 200 years, with years 51-200 used for analysis.

200 In this study the baseline simulation (piC) and the BC perturbation simulations of
 201 three different regions at the pre-industrial climate conditions (280 ppmv) were
 202 performed to explore potential physical processes of Asian BC aerosols influencing the
 203 local climate (Table 1). There is no significant difference in Asian climate responses to
 204 BC aerosols at different background climate states in the SyRAP-FORTE2 simulations
 205 (Stjern et al., 2024). The regional annual mean BC AOD perturbation is about 0.015 for
 206 East China, and about 0.01 for India, respectively (Figure 1a in Stjern et al., 2024). Note
 207 that only climate impacts due to ARI were considered here.

208 **2.3 Analysis methods and Datasets**

209 The response to a particular regional forcing is estimated by the mean difference
 210 between the perturbation simulation and the baseline simulation. Statistical significance
 211 of the response is assessed using a two-tailed Student's t-test.

212 The atmospheric energy budget is applied to understand the precipitation
 213 responses (Muller and O'Gorman, 2011; Richardson et al., 2016; Liu et al., 2018). The
 214 energy associated with precipitation can be separated into a thermodynamic component
 215 with only changes in the diabatic cooling (Q), and a dynamic component with only
 216 changes in the dry static energy (DSE) flux divergence (H), as shown in Eq. (1):

$$217 \quad L_c \delta P = \delta Q + \delta H \quad (1)$$

218 where L_c is the latent heat of condensation, P is precipitation, δ denotes a perturbation.

219 Then,

$$220 \quad \delta Q = \delta LWC - \delta SWA - \delta SH \quad (2)$$

221 where LWC is atmospheric longwave cooling, SWA is atmospheric shortwave



222 absorption, and SH is sensible heat flux from the surface.

223 δH is calculated as a residual between $L_c \delta P$ and δQ . Furthermore, H can be seen
 224 as the sum of the changes in mean (H_m) and eddy (H_{trans}) components. δH_m can be
 225 decomposed into four components associated with dynamic and thermodynamic effects
 226 on vertical and horizontal advection of DSE, as shown in Eq. (3):

$$\begin{aligned} 227 \quad \delta H_m &= \delta H_{Dyn_v} + \delta H_{Thermo_v} + \delta H_{Dyn_h} + \delta H_{Thermo_h} \\ 228 \quad &= \int \delta \bar{\omega} \frac{\partial \bar{s}}{\partial p} \frac{dp}{g} + \int \bar{\omega} \delta \left(\frac{\partial \bar{s}}{\partial p} \right) \frac{dp}{g} + \int \delta \bar{u} \cdot \nabla \bar{s} \frac{dp}{g} + \int \bar{u} \cdot \delta (\nabla \bar{s}) \frac{dp}{g} \quad (3) \end{aligned}$$

229 where ω is vertical velocity, s is DSE, p is pressure, g is the gravitational acceleration,
 230 u is horizontal wind vector, ∇ is the horizontal gradient, and an overbar indicates
 231 climatological monthly means. Therefore, H_{Dyn_v} is related to changes in vertical
 232 velocity, H_{Thermo_v} is related to changes in vertical DSE gradients, H_{Dyn_h} is related to
 233 changes in horizontal winds, and H_{Thermo_h} is related to changes in horizontal DSE
 234 gradients. δH_{trans} is calculated as a residual between δH and δH_m .

235 To evaluate the ability of FORTE2 to represent the observed climate monthly
 236 precipitation, surface temperature (T_s), and horizontal wind components were used
 237 from the NOAA-CIRES-DOE 20th Century Reanalysis V3 (20CR) on a $2^\circ \times 2^\circ$ grid
 238 spanning 1836 to 2015 (Compo et al., 2011). The 20CR is only based on surface
 239 observations of synoptic pressure of NOAA's physical Sciences Laboratory. Monthly
 240 sea level pressure (SLP) data were from the Hadley Centre (HadSLP) in a horizontal
 241 resolution of $5^\circ \times 5^\circ$ (Allan & Ansell, 2006).

242 To compare the response of FORTE2 to BC perturbations to the responses from
 243 CMIP class models we used the PDRMIP 10 times the modern Asian BC
 244 concentrations/emissions perturbation simulations and the baseline simulations with
 245 modern aerosol concentrations/emissions and greenhouse gases with the year 2000,
 246 based on the 5 GCMs (CESM1-CAM5, GISS-E2-R, HadGEM3, MIROC, and
 247 NorESM1; Table S1). More details of the PDRMIP design can be found in Myhre et al.
 248 (2017), while an overview of the monsoon response is given in Liu et al. (2018).

249 **3. Results**



250 **3.1 Evaluation of baseline climate in SyRAP-FORTE2**

251 Blaker et al. (2021) present a detailed overview of the FORTE2 climatology. The
 252 model simulates the Asian climate well, and the more focused evaluation presented by
 253 Stjern et al. (2024) demonstrated that FORTE2 is an appropriate tool to study the Asian
 254 climate effects of local aerosol perturbations. Here, for completeness, we present an
 255 overview of the skill of FORTE2 in simulating the Asian climate. The seasonal
 256 evolutions of precipitation and surface temperature (Ts) in East China and India, and
 257 the climatology of lower tropospheric circulation (SLP and 850 hPa horizontal wind)
 258 in the baseline experiment (piC) are compared with those in the reanalyses from 1851
 259 to 1896. FORTE2 reproduces the seasonality of precipitation in East China reasonably
 260 well, but slightly overestimates the averaged magnitude with about 1 mm/day in
 261 summer (Fig. 1a). However, the model underestimates the magnitude of South Asian
 262 Summer Monsoon precipitation by approximately 4 mm/day during June-September
 263 relative to the 20CR reanalysis. Dry biases in Indian summer precipitation of similar
 264 magnitudes are found in many CMIP5 and CMIP6 models (Sperber et al., 2013; Wilcox
 265 et al., 2020; Liu et al., 2024). Differences between reanalyses and observational datasets
 266 can also have similar magnitudes (Wilcox et al., 2020). Hence, we conclude that the
 267 FORTE2 representation of monsoon precipitation is suitable for our study. The model
 268 performs fairly well in the seasonality of temperature and the magnitudes in both
 269 regions (Fig. 1b).

270 The simulated SLPs are generally lower than that in HadSLP in all four seasons,
 271 especially the Siberian High in winter, the western North Pacific Subtropical High
 272 (WPSH) and the Indian Low in summer (Fig. 1c-j). Compared to the reanalyses, the
 273 simulated Indian Low is too strong, and its eastern fringe and the westerly from the
 274 Indian Ocean extend too far east into the western North Pacific, so does the Indian
 275 summer monsoon trough (Fig. 1g and h). This corresponds the model dry bias over the
 276 Indian subcontinent (Fig. 1a and S1e-f). Meanwhile, the WPSH is too weak to expand
 277 sufficiently far west, corresponding to the very weak easterly along the southern fringe
 278 of the WPSH, which lead to relatively less rainfall over the Philippines (Fig. S1e-f) and
 279 underestimate of the effects of the WPSH on the East Asian summer monsoon (Fig. 1g-



h). Despite these deficiencies, the model captures the essential features of lower tropospheric circulation, precipitation and temperature over Asia, which is consistent with Stjern et al. (2024).

3.2 Temperature and Precipitation responses

Figure 2 shows spatial patterns of Ts responses to increased Asian BC aerosols in four seasons. Firstly, there is a substantial land cooling over the perturbed regions in all four seasons, but with distinct seasonal differences in distributions and values. Under BC_CHI, a cooling can be seen in most of China in winter and spring (Fig. 2a-b), with the area-averaged values of -0.9 ± 1.2 K (mean value \pm 1 standard deviation) and -1.1 ± 0.9 K, respectively (Fig. 3a). The large standard deviations indicate the large spread of distributions of responses (Fig. S2). There is a slight warming of sea surface temperatures near China in spring. In summer and autumn, a cooling is seen mainly in the region to the north of the Yangtze River valley, especially in North China, while there is a weak warming to the south (Fig. 2c-d). The area-averaged values therefore are relatively smaller than those in winter and spring, showing about -0.7 ± 0.7 K for summer and autumn (Fig. 3a).

Under BC_IND, the strongest cooling occurs in the whole India in spring with the area-averaged value of -1.4 ± 1.4 K, but a weak warming in the tropical Indian Ocean (Fig. 2f and 3b). The significant cooling is concentrated in northern India in the other three seasons, with the area-averaged Ts decreased by 0.9 ± 1.3 K for winter and autumn, 0.6 ± 1.1 K for summer (Fig. 2e, g, h and 3b). The ocean surrounding the Indian subcontinent shows a smaller cooling in the three seasons.

Secondly, the BC perturbations not only cause the local responses, but also non-local responses through atmospheric circulations. The increased BC over East China leads to a dipolar pattern in India with a warming to the north and a cooling to the south in summer and autumn, and a significant warming in Central Asia in summer and Southeast Asia in autumn (Fig. 2c-d). BC emissions over India can induce a cooling in Southeast Asia in all seasons, and in summer the responses are the strongest with the averaged value of about 1.15 K. Meanwhile, there is a significant cooling in central and



southern China in summer and autumn, with decreases of 0.3 ± 0.7 K and 0.2 ± 0.7 K, respectively (Fig. 2g-h and 3a). These added impacts lead to an East Asian cooling response under BC_CHI+IND that is stronger than that under BC_CHI in summer and autumn (Fig. 2k-l and 3a). Moreover, by comparing the responses to both regions at once to the sum of responses to the two separate regions, it is found that the differences are almost insignificant, suggesting that the impact of Asian BC aerosol on the Asian Ts is linear regionally in all four seasons (Fig. S3).

In contrast to Ts responses, the responses in air temperature (Ta) at 850 hPa show a significant warming over much of the perturbed regions (Fig. 3c-d and 4). A cooling occurs over a few perturbed regions, such as central China under BC_CHI and BC_CHI+IND in winter (Fig. 4a, i). The vertical distribution of the temperature response is characterized by cooling at the surface and warming in the lower troposphere. This is a result of atmospheric absorption of solar shortwave radiation (SW) by BC aerosols, and is consistent with many previous studies (e.g., Li et al., 2016). Outside the perturbed regions, the Ta responses are in line with the Ts response, for example a cooling over China and Southeast Asia under BC_IND in summer and autumn (Fig. 3c and 4g, h).

Increased BC over East China primarily induces robust drying over most of China in all four seasons (Fig. 3e and 5a-d). Specifically, the spatial distribution in summer shows a substantial decrease over southern China (up to 40%), a relatively weaker decrease over north China and a weak increase over northwest China, with the area-averaged precipitation decreased by 0.5 ± 0.5 mm/day (Fig. 3e, 5c and S4c). In spring and autumn, the decreased precipitation is mainly located in south and northeast China by up to about 40% (Fig. 5b and d). Although the absolute change is the weakest in winter (-0.2 ± 0.3 mm/day), the relative change in central China decreases by up to about 60% (Fig. 3e, 5a and S4a). Under BC_IND, the response over the Indian subcontinent is only statistically significant in summer, with a decrease of 0.5 ± 1.1 mm/day ($\sim 21\%$) (Fig. 3f and 5g).

Additionally, under BC_CHI there is increased rainfall over India in summer and autumn, which can counteract the local decrease due to Indian BC forcing (Fig. 3f and



339 5c-d). Hence, when considering the simultaneous BC forcing in the two regions
 340 (BC_CHI+IND) in summer and autumn, there is no significant change in the regional
 341 mean, showing a dipolar pattern with more rainfall over northern India and less rainfall
 342 over southern India (Fig. 3f and 5k-l). On the other hand, BC_IND can induce a
 343 significant precipitation increase over China and Southeast Asia in spring and summer
 344 (Fig. 5f-g), and partly offset the decrease in response to BC_CHI over China. Hence,
 345 there are weaker responses under BC_CHI+IND for China than those under BC_CHI
 346 (Fig. 3e). For regional linearity, the responses are almost linear (Fig. S5). Only few
 347 regions exhibit nonlinear response, such as a decrease over south Thailand in winter, an
 348 increase over northeast India in spring and summer. The above analysis regarding
 349 summer part has been included in Stjern et al. (2024), but is included here as a precursor
 350 to the detailed mechanistic analysis that follows.

351 **3.3 Energy balance response**

352 The following analysis mainly focuses on summer for clarity; the results in the
 353 other three seasons are in the supplement (Figures S7-S10, S12-S16). The spatial
 354 patterns of net TOA and surface energy responses to regional BC aerosols in summer
 355 are illustrated in figure 6. As expected, there are increases in net downward TOA
 356 shortwave (SW) with area mean responses of 7.3~9.6 W/m² associated with decreases
 357 in convective clouds over the perturbed regions (Fig. 6a-c and S6j-l). Decreases in net
 358 surface downward SW can be seen with area mean responses of -22.6~-27.8 W/m² due
 359 to SW absorption by BC aerosols (Fig. 6d-f). Significant increases in low and middle
 360 clouds also contribute to the reduction in surface SW (Fig. S6d-i). Hence, there is
 361 warming in the troposphere and cooling at surface in these perturbed regions. The
 362 enhanced net surface upward longwave (LW) has a small contribution to the local
 363 surface cooling with area mean responses from -3.2 to -5.8 W/m² (Fig. 6g-i), which is
 364 related to the decreases in convective clouds (Fig. S6j-l). On the contrary, the positive
 365 changes in downward sensible heat (SH) (8.1~9.8 W/m²) and latent heat (LH) (9.5~12.9
 366 W/m²) cause a warming effect partly offsetting the cooling in the perturbation regions
 367 (Fig. 6j-o). The decreased SH is caused by the vertical temperature differences between



the surface and lower atmosphere, and the decreased LH associated with heating aloft and precipitation. Outside the perturbation regions, the negative changes in SW, LW and LH are responsible for the cooling in Southeast Asia and south China induced by the increased BC in India (Fig. 6e, h, n). Similar results can be seen in other three seasons (Table S2).

Figure 7 shows area-averaged atmospheric column energy budget terms (see Eq. 1) over East China and India in summer. For the drying in East China/India under BC_CHI/BC_IND, the substantial reductions of the diabatic cooling (δQ) are the prime driver of the decreases in the energy of precipitation ($L_c\delta P$), while the increases in the DSE flux divergence (δH) offset the effect of δQ to a large extent.

The enhanced precipitation in China under BC_IND, and in India under BC_CHI, is the result of increased δH (blue and green bars in Fig. 7 are almost identical), with negligible contribution from δQ . Hence, the local precipitation response to local BC increases is largely driven by δQ , while the remote precipitation response is largely driven by δH . Consequently, it can be found that the larger changes in δH lead to the smaller responses in $L_c\delta P$ over China and India under BC_CHI+IND, relative to the changes under BC_CHI and BC_IND. It should be mentioned that the relatively large uncertainties (error bars in Fig. 7) of $L_c\delta P$ mainly depend on δH . The other three seasons show the similar results (Fig. S7).

Spatially, δQ shows a significant decrease throughout the entire perturbed regions in the three simulations, with large decreases located over North China and northern India (Fig. 8d-f). Under BC_CHI, δH is characterized by a dipolar pattern with positive changes in north of the Yangtze River and negative in south (Fig. 8g). Hence, δH and δQ cancel each other out in North and Northeast China, and combine with each other in south of the Yangtze River. As a result, there is the strongest decrease in precipitation in south China, and relatively weak decrease in north China (Fig. 8a). Under BC_IND, significant positive changes in δH can be found along the southern edge of Himalayas and the southern tip of the Indian subcontinent, and weak and nonsignificant negative changes in central India (Fig. 8h). δH can therefore offset the negative changes in δQ in north and south India. The substantial $L_c\delta P$ reduction is concentrated in central India



398 mainly due to δQ (Fig. 8b).

399 In addition, δH is the dominating factor for $L_c \delta P$ beyond the perturbation regions,
 400 for example positive changes in northeast India under BC_CHI, positive changes from
 401 Southeast Asia to the tropical western Pacific and central China under BC_IND (Fig.
 402 8g-h). Under BC_CHI+IND, it can be found that the extent and magnitude of δH are
 403 larger than those in the simulations of individual regions (Fig. 8i), which indicates more
 404 balance between δH and δQ , corresponding to relatively weaker precipitation over East
 405 China and India (Fig. 7 and 8c). Relative to summer, δQ and δH has negative and
 406 positive changes in the whole perturbation regions in the other three seasons,
 407 respectively (Fig. S8-10). In winter and spring, there is a marked seesaw pattern of δH
 408 between Asia and the tropical Indian Ocean and maritime continent under
 409 BC_CHI+IND, leading to less precipitation in the latter regions (Fig. S8c, i and S9c, i).
 410 Overall, the combined effect of δH and δQ shape the spatial pattern of precipitation
 411 responses to the regional BC.

412 The reductions in δQ (see Eq. 2) are dominated by the strong atmospheric heating
 413 due to SW absorption by BC aerosols ($-\delta SWA$), and also contributed by the small
 414 decreases in the atmospheric longwave cooling (δLWC) (Fig. S11a-f). The sensible heat
 415 flux from the surface ($-\delta SH$) plays a role in increasing δQ , but with relatively small
 416 values (Fig. S11g-i).

417 **3.4 Dynamic processes responsible for responses**

418 Due to storage constraints, 3D atmospheric output from FORTE2 was archived on
 419 three pressure levels, 250 hPa, 500 hPa, and 850hPa, to capture three key aspects of the
 420 tropospheric circulation response. While this precludes a quantitative analysis of the
 421 component terms of δH_m (Eq. 3), it is sufficient to identify to main contributing term.
 422 We now examine the four terms of δH_m (see Eq. 3), including the dynamic components
 423 with changes in vertical and horizontal atmospheric circulations ($\delta H_{D_{yn_v}}$ and $\delta H_{D_{yn_h}}$),
 424 and thermodynamic components with changes in vertical and horizontal DSE gradients
 425 (δH_{Thermo_v} and δH_{Thermo_h}). Figure 9 displays spatial patterns of the four components



426 in summer in the three simulations. In general, the δH_{Dyn_v} highly resembles the δH in
 427 the three simulations, and the magnitudes in δH_{Dyn_v} are far greater than those in the
 428 other three terms, suggesting that dynamic effect of vertical circulation is the primary
 429 contributor to δH (Fig. 9a-c). $\delta H_{\text{Thermo}_v}$ and δH_{Dyn_h} are small in all regions for all
 430 experiments. Larger anomalies are seen in $\delta H_{\text{Thermo}_h}$, where negative anomalies offset
 431 some of the influence of δH_{Dyn_v} over the Indo-China peninsula in the BC_IND and
 432 BC_CHI+IND experiments. However, these anomalies are not sufficient to influence
 433 the sign of δH , which is still primarily driven by δH_{Dyn_v} in this region. In the other
 434 seasons, δH_{Dyn_v} remains the most important factor (Fig. S12-14), although it is more
 435 strongly offset by δH_{Dyn_h} and $\delta H_{\text{Thermo}_h}$ in winter. The effects of horizontal
 436 circulation are relatively weak in spring and autumn.

437 Based on the above analysis, we conclude that vertical movement is the most
 438 important contributor to δH_m . As expected, the spatial patterns of responses in Omega
 439 (vertical velocity) at 500 hPa correspond well to those in δH_{Dyn_v} (Fig. 10a-c).
 440 Anomalous ascent corresponds to the increase in δH_{Dyn_v} , leading to more precipitation,
 441 which offsets the precipitation reduction driven by decreased δQ . Anomalous descent
 442 suppresses precipitation, adding to the precipitation reduction driven by the reduction
 443 in δQ .

444 Why does the vertical velocity exhibit such changes? It seems to be related to the
 445 temperature responses in the troposphere, reflected by a good corresponding
 446 relationship between the Omega and Ta responses at 500 hPa (Fig. 10a-f). The warm
 447 anomalies favor a divergence in the middle troposphere, which in turn are associated
 448 with anomalous ascent. The cold anomalies are associated with a convergence and
 449 descending motion. The above-mentioned relationship also exists in the other seasons,
 450 and it is more pronounced at 850 hPa (Fig. 4 and S15).

451 From the transects of zonal mean diabatic heating over the perturbation regions,
 452 changes to tropospheric heating can be seen more clearly (Fig. 11). Under BC_CHI, the



453 responses in diabatic heating show a meridional dipolar structure through the whole
 454 troposphere over East China, with a cooling over the region to south of 32°N (the
 455 Yangtze River basin), and a warming to north (Fig. 11a). The dipolar pattern
 456 corresponds well to the meridional distributions of precipitation, vertical velocity and
 457 Ta at 500 hPa. The cooling center located at the middle troposphere is due to the reduced
 458 latent heat release caused by the substantial decrease in precipitation over south China.
 459 The heating center at the lower troposphere in the north mainly results from SW
 460 absorption by increased BC aerosol. The difference between south China and north
 461 China is associated with the larger AOD perturbation imposed north of the Yangtze
 462 basin in SyRAP-FORTE2 (Stjern et al., 2024). In BC_CHI+IND, there is a similar
 463 dipolar pattern, except for a warming at the lower troposphere around south of 30°N
 464 (Fig. 11b). The warming is related to the increased precipitation over south China
 465 because of the BC aerosols over India.

466 For India in BC_IND, there is also a cooling center associated with the reduced
 467 precipitation in the middle troposphere (Fig. 11c), corresponding to a cold anomaly and
 468 descending motion at 500 hPa (Fig. 10b, e). In the lower troposphere, a warming can
 469 be seen at south of the Qinghai-Tibet Plateau. Compared with BC_IND, the cold
 470 anomaly is weaker, but the warm anomalies are strengthened under BC_CHI+IND (Fig.
 471 11d). Hence, a significant ascending motion can be found in northeast India resulted
 472 from the effect of increased BC over East Asia (Fig. 10c), which is consistent with that
 473 in Herbert et al. (2022). In the other three seasons, however, unlike in summer, there is
 474 no cooling center in the middle troposphere, and the heating centers are situated at the
 475 lower troposphere (Fig. S16). Overall, the diabatic heating induced by the increased BC
 476 aerosols at the lower troposphere leads to an ascending motion explaining the increased
 477 δH over the perturbation regions.

478 Considering that the dynamic and thermodynamic effects of horizontal
 479 atmospheric circulations have some contributions to δH , we look at the changes in
 480 lower tropospheric horizontal circulation in response to changes of regional BC
 481 aerosols (Fig. 10g-i). Under BC_CHI, the cyclone anomaly over East China leads to
 482 anomalous easterly wind over North China with cutting off the moisture supply from



483 south (Fig. 10g). Under BC_IND, the westerly anomalies associated with the cyclonic
 484 circulation over India favor to strengthen the Indian summer monsoon, which corresponds
 485 to the increase in δH_{Dyn_h} (Fig. 10h). The responses in the circulations to both regions
 486 at once can be seen as the sum of responses to the two separate regions (Fig. 10i).
 487 Additionally, there is a cyclonic circulation over East China and an anticyclonic
 488 circulation over central China in winter under BC_CHI (Fig. S17), leading to
 489 anomalous northerly wind across central China and then suppress precipitation over
 490 there, which is in agreement with the decrease in δH_{Dyn_h} (Fig. S10g). The changes in
 491 horizontal circulations are related to the changes in Ta and omega in the lower
 492 troposphere (Fig. 4 and S15).

493 **4 Energy budget analysis in other coupled models**

494 To evaluate the precipitation response and the mechanisms in FORTE2, we
 495 compare the results of energy budget analysis (see Eq. 1) in the PDRMIP simulations
 496 forced by 10 times the present-day Asian BC concentrations/emissions in five CMIP-
 497 class models to those in the SyRAP-FORTE2 BC_CHI+IND experiment. Spatial
 498 patterns of summer energy budgets in the PDRMIP models are illustrated in Figure 12.
 499 There are significant decreases in δQ over most of Asia in all of the PDRMIP models,
 500 which is generally consistent with the results under BC_CHI+IND (Fig. 12f-j). Three
 501 models (CESM1-CAM5, GISS-E2-R and NorESM1) have similar distributions of δQ
 502 to BC_CHI+IND, showing a maximum center in North China and northern India. δH
 503 increases significantly in India and most of East China in these models (Fig. 12k, l, o),
 504 again roughly resembling the changes of BC_CHI+IND (Fig. 8i), while the other two
 505 models show a significant increase in north India and North China with weaker
 506 magnitudes (Fig. 12m-n). The PDRMIP multi-model mean changes in δH [figure 7 in
 507 Liu et al. (2018)] are also similar to the changes in BC_CHI+IND. In spite of these
 508 model differences in the individual terms, models are broadly consistent in their total
 509 $L_c\delta P$ responses. Precipitation generally increases over India and North China, and
 510 decrease over South China in the PDRMIP models and FORTE2 (Fig. 12a-e). There is



511 no significant increase in δH and precipitation in Southeast Asia in the PDRMIP models.

512 Figure 13 shows the regional means of each energy budget term over East China
 513 and India in summer under the PDRMIP models. There is a weak and insignificant
 514 reduction in $L_c\delta P$ from -0.6 (HadGEM3) to -7.2 W/m^2 (NorESM1) for East China,
 515 which are comparable to the value of -3.8 W/m^2 under BC_CHI+IND (Fig. 13a). Hence,
 516 the result under BC_CHI+IND in FORTE2 is agreement with the PDRMIP models,
 517 suggesting that the increased BC perturbations over Asia lead to slight decreases in
 518 precipitation over East China in all of the models. The regional means range from -1.2
 519 (MIROC) to 13.7 W/m^2 (NorESM1) for India (Fig. 13b). Except for MIROC, $L_c\delta P$ in
 520 the other models have stronger increases than that under BC_CHI+IND, about 0.6
 521 W/m^2 , which may be related to the larger drying bias of Indian summer precipitation in
 522 FORTE2.

523 The effect of δQ decreases $L_c\delta P$ with a large range from -4.7 (HadGEM3) to -29.8
 524 W/m^2 (GISS-E2-R) for East China, while δH has an opposite effect from 2.1 (MIROC)
 525 to 24.4 W/m^2 (GISS-E2-R) (Fig. 13a). Similarly, δQ changes from -5.7 (HadGEM3) to
 526 -25.8 W/m^2 (GISS-E2-R) for India, and δH from 4.9 (MIROC) to 36.5 W/m^2 (GISS-
 527 E2-R) (Fig. 13b). The magnitudes in δQ and δH under the PDRMIP models are much
 528 smaller than those in FORTE2 in both the two regions, except for GISS-E2-R. The
 529 negative effect of δQ and the positive effect of δH also can be seen in the PDRMIP
 530 multimodel mean for the whole Asian region (Liu et al., 2018). Despite large difference
 531 in the magnitudes of their responses, which are to be expected from their large range of
 532 aerosol radiative forcing and climatological precipitation, the results of these models
 533 are overall consistent qualitatively.

534 **5 Conclusion and Discussion**

535 In this study, we have investigated the Asian climatic responses to adding BC
 536 aerosols to the separate regions (East China and India), and both regions at once, and
 537 examined the associated physical processes, with the SyRAP simulations based on the
 538 reduced-complexity climate model FORTE2. Our main findings are as follows.

539 i. BC increases over East Asia or South Asia lead to a local strong surface cooling



540 and lower tropospheric air temperature warming in all four seasons, with seasonal
 541 differences in magnitude and spatial distribution. The responses in temperature are
 542 dominated by the substantial decreases in surface SW radiation due to SW absorption
 543 by BC aerosols. BC over East Asia causes significant drying in south and northeast
 544 China in spring, summer and autumn. In winter, there is a significant reduction in
 545 central China. BC over South Asia induces a substantial decrease in rainfall in India in
 546 summer. Also, South Asian BC induces significant decreases in temperature and
 547 precipitation in Southeast Asia in summer and autumn.

548 ii. Responses in temperature and precipitation to Asian BC forcing are mostly
 549 linear regionally in all four seasons. There are relatively smaller decreases in
 550 precipitation responses to adding BC over both regions simultaneously, compared to
 551 the local reductions in precipitation responses to BC increases over East Asia and South
 552 Asia separately. This is because BC over East Asia (BC over India) increases
 553 precipitation in northeast India, while BC over South Asia increases precipitation over
 554 southern and central China.

555 iii. Using an energy budget analysis, we find that reductions in the energy of local
 556 precipitation ($L_c \delta P$) over the perturbation regions result from decreases in net
 557 atmospheric diabatic cooling (δQ). The increases in the dry static energy (DSE) flux
 558 divergence (δH) play a role in offsetting the effects of δQ to a large extent.
 559 Consequently, the responses in precipitation to Asian BC can be considered as the result
 560 of interactions between thermodynamic and dynamic processes. For δQ , the reductions
 561 are mainly due to the strong atmospheric heating ($-\delta SWA$). For δH , the increases
 562 depend mainly on the positive changes in the dynamic processes associated with
 563 vertical atmospheric circulations (δH_{dyn_v}). We find that δH_{dyn_v} patterns correspond
 564 well to vertical velocity change patterns at the middle and lower troposphere.
 565 Anomalous ascent is primarily triggered by the warming in the middle and lower
 566 troposphere over north China in summer and in most of Asia in the other seasons.
 567 However, there is anomalous descent in southern China and central India in summer,
 568 which is a result of cool anomalies in the middle troposphere due to the reduced latent



569 heat release caused by the substantial decrease in precipitation. The difference in
 570 diabatic heating at the middle and lower troposphere is related to the difference in
 571 spatial distributions of AOD in the different seasons.

572 It is well known that the EASM and SASM underwent weakening trends during
 573 the second half of the 20th century (Wang et al., 2001; Bollasina et al., 2011). Although
 574 the variations of ASM have been attributed to many factors including internal
 575 variability and external forcing, the strong increases in BC emissions from East and
 576 South Asia (Lund et al., 2019) could play a role in weakening the ASM over the past
 577 decades according to this study. The increased BC also could alleviate the enhanced
 578 precipitation over south China due to GHG increase since the mid-1990s (Tian et al.,
 579 2018). Since the early 2010s, anthropogenic aerosols (including BC and sulfate) have
 580 been decreasing in East China, while they have continued to rise in India; trends which
 581 are expected to continue over the coming decades (Lund et al., 2019; Samset et al.,
 582 2019). Hence, there is a new dipole pattern characterized by decreasing aerosols over
 583 East China and increasing aerosols over India. Given that responses to Asian BC forcing
 584 are linear regionally in the SyRAP-FORTE2 simulations, the impacts of the dipole
 585 pattern on the Asian climate can be roughly estimated by the sum of responses to BC
 586 over China multiplied by -1 and responses to BC over India. The result shows that there
 587 are warm anomalies in north China and cold anomalies in south China, southeast Asia
 588 and most of India, and positive precipitation anomalies over most of China (especially
 589 south China) and southeast Asia, and negative anomalies over India (Fig. S18). It is
 590 overall consistent with the result in Xiang et al. (2023), although their result involves
 591 the combined effect of BC and sulfate.

592 Large differences in the magnitude and spatial pattern of precipitation responses
 593 to BC can be across models. The smaller precipitation responses over India in FORTE2
 594 relative to PDRMIP may partly be due to much larger BC perturbation in PDRMIP. Liu
 595 et al. (2024) have proposed that the responses of Asian summer rainfall to Asian
 596 aerosols are strongly modulated by regional precipitation biases. Some other factors or
 597 mechanisms may play a role in causing differences in responses to Asian BC, such as
 598 bias of atmospheric circulations, land-atmosphere interaction. Further work to



599 understand the mechanisms behind model differences in the response to BC would help
600 to reduce uncertainties and would improve the confidence in future Asian climate
601 change projections.

602 **Acknowledgements.** This work is supported by the Second Tibetan Plateau Scientific
603 Expedition and Research Program (2019QZKK010203). Some of the research
604 presented in this paper was carried out on the High Performance Computing Cluster
605 supported by the Research and Specialist Computing Support service at the University
606 of East Anglia. We acknowledge the Center for Advanced Study in Oslo, Norway that
607 funded and hosted our HETCLIF centre during the academic year of 2023/24. F. L. is
608 supported by the Scientific Research of Chengdu University of Information Technology
609 (Grant No. KYTZ202210). B. H. S., C. W. S., L. J. W., M. J. and R. J. A were supported
610 by the Research Council of Norway [Grant 324182 (CA3THY)].

611 **Data availability.** The NOAA-CIRES-DOE 20th Century Reanalysis V3 (20CR)
612 datasets are obtained from https://psl.noaa.gov/data/gridded/data.20thC_ReanV3.html.
613 The HadSLP2r is provided by the UK Met Office Hadley Centre and can be
614 downloaded from at <http://www.metoffice.gov.uk/hadobs/hadslp2/>. The PDRMIP data
615 can be accessed through the World Data Center for Climate (WDCC) data server at
616 https://doi.org/10.26050/WDCC/PDRMIP_2012-2021. Data of the SyRAP-FORTE2
617 experiments reported in this paper are available without restriction on reasonable
618 request from Camilla W. Stjern at CICERO Center for International Climate Research.

619 **Author contribution.** F. L. and B. H. S. designed the study. C. W. S., L. J. W., M. J.
620 ran the model simulations. F. L. carried out the analysis and visualized the results. All
621 authors discussed the results and edited the paper.

622 **Competing interests.** L. J. W. is a member of the editorial board of *Atmospheric*
623 *Chemistry and Physics*.

624 **References**

625 Allan, R. and Ansell, T.: A new globally-complete monthly historical gridded mean sea



- 626 level pressure dataset (HadSLP2): 1850-2004, *J. Climate*, 19, 5816-5842,
 627 <https://doi.org/10.1175/JCLI3937.1>, 2006.
- 628 Betts, A. K. and Miller, M. J.: The Betts-Miller scheme, in: *The Representation of*
 629 *Cumulus Convection in Numerical Models of the Atmosphere*, Chapter 9, edited
 630 by: Emanuel, K. A. and Raymond, D. J., *Amer. Meteor. Soc., Meteor. Mon.*, 24,
 631 107-121, 1993.
- 632 Blaker, A. T., Joshi, M., Sinha, B., Stevens, D. P., Smith, R. S., and Hirschi, J. J.-M.:
 633 FORTE 2.0: a fast, parallel and flexible coupled climate model, *Geosci. Model*
 634 *Dev.*, 14, 275-293, 10.5194/gmd-14-275-2021, 2021.
- 635 Bollasina, M. A., Ming, Y. and Ramaswamy, V.: Anthropogenic aerosols and the
 636 weakening of the South Asian summer monsoon, *Science*, 334, 502-505,
 637 <https://doi.org/10.1126/science.1204994>, 2011.
- 638 Bond, T. C., Doherty, S. J., Fahey, D. W., Forster, P., Berntsen, T., DeAngelo, B.,
 639 Flanner, M., Ghan, S., Kähler, B., Koch, D., Kinne, S., Kondo, Y., Quinn, P. K.,
 640 Sarofim, M. C., Schultz, M. G., Schulz, M., Venkataraman, C., Zhang, H., Zhang,
 641 S., Bellouin, N., Guttikunda, S. K., Hopke, P. K., Jacobson, M. Z., Kaiser, J. W.,
 642 Klimont, Z., Lohmann, U., Schwarz, J. P., Shindell, D., Storelvmo, T., Warren, S.
 643 G., and Zender, C. S.: Bounding the role of black carbon in the climate system: A
 644 scientific assessment, *J. Geophys. Res.-Atmos.*, 118, 5380-552, 2013.
- 645 Chen, H., Zhuang, B., Liu, J., Li, S., Wang, T., Xie, X., Xie, M., Li, M. and Zhao, M.:
 646 Regional Climate Responses in East Asia to the Black Carbon Aerosol Direct
 647 Effects from India and China in Summer, *J. Climate*, 33, 9783-9800,
 648 <https://doi.org/10.1175/JCLI-D-19-762> 0706.1, 2020.
- 649 Compo, G. P., Whitaker, S., Sardeshmukh, J., Matsui, N., Allan, R. J., Yin, X., Gleason,
 650 B. E., Vose, R. S., Rutledge, G., Bessemoulin, P., Brönnimann, S., Brunet,
 651 M., Crouthamel, R. I., Grant, A. N., Groisman, P. Y., Jones, P. D., Kruk, M.
 652 C., Kruger, A. C., Marshall, G. J., Maugeri, M., Mok, H. Y., Nordli, Ø., Ross, T.
 653 F., Trigo, R. M., Wang, X. L., Woodruff, S. D. and Worley, S. J.: The Twentieth
 654 Century Reanalysis Project, *Q. J. Roy. Meteor. Soc.*, 137, 1-28, 2011.
- 655 Deng, J., Xu, H., Ma, H., Jiang Z.: Numerical study of the effect of anthropogenic



- 656 aerosols on spring persistent rain over eastern China, *J. Meteorol. Res.*, 28, 341-
 657 353, 2014.
- 658 Dong, B., Wilcox, L. J., Highwood, E. J., and Sutton, R. T.: Impacts of recent decadal
 659 changes in Asian aerosols on the East Asian summer monsoon: roles of aerosol-
 660 radiation and aerosol-cloud interactions, *Clim. Dyn.*, 53, 3235–3256,
 661 <https://doi.org/10.1007/s00382-019-04698-0>, 2019.
- 662 Gu, Y., Liou, K. N., Xue, Y., Mechoso, C. R., Li, W. and Luo, Y.: Climatic effects of
 663 different aerosol types in China simulated by the UCLA general circulation model,
 664 *J. Geophys. Res.*, 111, D15201, doi:10.1029/2005JD006312, 2006.
- 665 Guo, L., Highwood, E. J., Shaffrey, L. C. and Turner, A. G.: The effect of regional
 666 changes in anthropogenic aerosols on rainfall of the East Asian Summer Monsoon,
 667 *Atmos. Chem. Phys.*, 13, 1521-1534, <https://doi.org/10.5194/acp-13-1521-2013>,
 668 2013.
- 669 Guo, L., Turner, A. and Highwood, E.: Impacts of 20th century aerosol emissions on
 670 the South Asian monsoon in the CMIP5 models, *Atmos. Chem. Phys.*, 15, 6367-
 671 6378, <https://doi.org/10.5194/acp-15-6367-2015>, 2015.
- 672 Herbert, R., Wilcox, L. J., Joshi, M., Highwood, E. and Frame, D.: Nonlinear response
 673 of Asian summer monsoon precipitation to emission reductions in South and East
 674 Asia, *Environ. Res. Lett.*, 17, 014005, 10.1088/1748-9326/ac3b19, 2022.
- 675 Hu, N. and Liu, X.: Modeling study of the effect of anthropogenic aerosols on late
 676 spring drought in South China, *Acta Meteorol. Sin.*, 27, 701-715,
 677 doi:10.1007/s13351-013-0506-z, 2014.
- 678 Inness, A., Ades, M., Agustí-Panareda, A., Barré, J., Benedictow, A., Blechschmidt, A.-
 679 M., Dominguez, J. J., Engelen, R., Eskes, H., Flemming, J., Huijnen, V., Jones, L.,
 680 Kipling, Z., Massart, S., Parrington, M., Peuch, V.-H., Razinger, M., Remy, S.,
 681 Schulz, M., and Suttie, M.: The CAMS reanalysis of atmospheric composition,
 682 *Atmos. Chem. Phys.*, 19, 3515-3556, 10.5194/acp-19-3515-2019, 2019.
- 683 IPCC, 2021: Climate Change 2021: The Physical Science Basis. Contribution of
 684 Working Group I to the Sixth Assessment Report of the Intergovernmental Panel
 685 on Climate Change [Masson-Delmotte, V., P. Zhai, A. Pirani, S.L. Connors, C.



- 686 Péan, S. Berger, N. Caud, Y. Chen, L. Goldfarb, M.I. Gomis, M. Huang, K. Leitzell,
 687 E. Lonnoy, J.B.R. Matthews, T.K. Maycock, T. Waterfield, O. Yelekçi, R. Yu, and
 688 B. Zhou (eds.)). Cambridge University Press, Cambridge, United Kingdom and
 689 New York, NY, USA, 2391 pp. doi:10.1017/9781009157896.
- 690 Jiang, Y., Liu, X., Yang, X. Q. and Wang, M.: A numerical study of the effect of different
 691 aerosol types on East Asian summer clouds and precipitation, *Atmos. Environ.*, 70,
 692 51-63, 2013.
- 693 Jiang, Y., Yang, X. Q., Liu, X., Yang, D., Sun, X., Wang, M., Ding, A., Wang, T. and Fu,
 694 C.: Anthropogenic aerosol effects on East Asian winter monsoon: The role of black
 695 carbon-induced Tibetan Plateau warming, *J. Geophys. Res. Atmos.*, 122, 5883-
 696 5902, doi:10.1002/2016JD026237, 2017.
- 697 Joshi, M., Stringer, M., van der Wiel, K., O'Callaghan, A. and Fueglistaler, S.: IGCM4:
 698 a fast, parallel and flexible intermediate climate model, *Geosci. Model Dev.*, 8,
 699 1157-1167, 10.5194/gmd-8-1157-2015, 2015.
- 700 Lau, K. M., Kim, M. K. and Kim, K. M.: Asian monsoon anomalies induced by aerosol
 701 direct forcing: the role of the Tibetan Plateau, *Clim. Dynam.*, 26, 855-664, 2006.
- 702 Lau, K. M. and Kim, K. M.: Does aerosol strengthen or weaken the Asian monsoon? in
 703 *Mountains: Witnesses of Global Change*, edited by: Baudo, R., Tartari, G., and
 704 Vuillermoz, E., Elsevier, Amsterdam, the Netherlands, 2007.
- 705 Li, J., Carlson, B. E., Yung, Y. L., Lv, D., Hansen, J., Penner, J., Liao, H., Ramaswamy,
 706 V., Kahn, R., Zhang, P., Dubovik, O., Ding, A., Lacis, A., Zhang, L. and Dong,
 707 Y.: Scattering and absorbing aerosols in the climate system, *Nat. Rev. Earth.*
 708 *Environ.*, 3, 363-379, <https://doi.org/10.1038/s43017-022-00296-7>, 2022.
- 709 Li, Z., Lau, W. K., Ramanathan, V., Wu, G., Ding, Y., Manoj, M. G., Liu, J., Qian, Y.,
 710 Li, J., Zhou, T., Fan, J., Rosenfeld, D., Ming, Y., Wang, Y., Huang, J., Wang, B.,
 711 Xu, X., Lee, S. S., Cribb, M., Zhang, F., Yang, X., Takemura, T., Wang, K., Xia,
 712 X., Yin, Y., Zhang, H., Guo, J., Zhai, P. M., Sugimoto, N., Babu, S. S., and Brasseur,
 713 G. P.: Aerosol and Monsoon Climate Interactions over Asia, *Rev. Geophys.*, 54,
 714 866–929, <https://doi.org/10.1002/2015rg000500>, 2016.
- 715 Liu, L., Shawki, D., Voulgarakis, A., Kasoar, M., Samset, B. H., Myhre, G., Forster, P.



- 716 M., Hodnebrog, Ø, Sillmann, J., Aalbergstjø, S. G., Boucher, O., Faluvegi, G.,
 717 Iversen, T., Kirkevåg, A., Lamarque, J., Olivié, D., Richardson, T., Shindell, D.
 718 and Takemura, T.: A PDRMIP Multimodel Study on the Impacts of Regional
 719 Aerosol Forcings on Global and Regional Precipitation, *J. Climate*, 31, 4429-4447,
 720 <https://doi.org/10.1175/JCLI-D-17-0439.1>, 2018.
- 721 Liu, Z., Bollasina, M. and Wilcox, L.: Impact of Asian aerosols on the summer monsoon
 722 strongly modulated by regional precipitation biases, *EGUsphere* [preprint],
 723 <https://doi.org/10.5194/egusphere-2023-3136>, 2024.
- 724 Lou, S., Yang, Y., Wang, H., Lu, J., Smith, S., Liu, F. and Rasch, P.: Black Carbon
 725 Increases Frequency of Extreme ENSO Events, *J. Climate*, 32, 8323-33,
 726 <https://doi.org/10.1175/JCLI-D-19-0549.1>, 2019.
- 727 Lou, S., Yang, Y., Wang, H., Smith, S., Qian, Y. and Rasch, P.: Black carbon amplifies
 728 haze over the North China Plain by weakening the East Asian winter monsoon,
 729 *Geophys. Res. Lett.*, 46, 452-460, <https://doi.org/10.1029/2018GL080941>, 2019.
- 730 Lund, M. T., Myhre, G. and Samset, B. H.: Anthropogenic aerosol forcing under the
 731 Shared Socioeconomic Pathways, *Atmos. Chem. Phys.*, 19, 13827-13839,
 732 <https://doi.org/10.5194/acp-19-13827-2019>, 2019.
- 733 Mahmood, R. and Li, S.: Remote influence of South Asian black carbon aerosol on East
 734 Asian summer climate, *Int. J. Clim.*, 34, 36-48, <https://doi.org/10.1002/joc.3664>,
 735 2014.
- 736 Meehl, G. A., Arblaster, J. M. and Collins, W. D.: Effects of black carbon aerosols on
 737 the Indian monsoon, *J. Climate*, 21, 2869-2882,
 738 <https://doi.org/10.1175/2007JCLI1777.1>, 2008.
- 739 Muller, C. J. and O’Gorman, P. A.: An energetic perspective on the regional response
 740 of precipitation to climate change. *Nat. Climate Change*, 1, 266-271,
 741 <https://doi.org/10.1038/nclimate1169>, 2011.
- 742 Menon, S., Hansen, J., Nazarenko, L., Nazarenko, L. and Luo, Y.: Climate effects of
 743 black carbon aerosols in China and India, *Science*, 297, 2250-2253, 2002.
- 744 Myhre, G., Forster, P., Samset, B., Hodnebrog, Ø, Sillmann, J., Aalbergstjø, S. G.,
 745 Andrews, T., Boucher, O., Faluvegi, G. and Flächner, D.: PDRMIP: A precipitation



- 746 driver and response model intercomparison project, protocol and preliminary
 747 results, *B. Am. Meteorol. Soc.*, 98, 1185-1198, [https://doi.org/10.1175/BAMSD-](https://doi.org/10.1175/BAMSD-16-0019.1)
 748 16-0019.1, 2017.
- 749 Persad, G. G., Paynter, D. J., Ming, Y. and Ramaswamy, V.: Competing Atmospheric
 750 and Surface-Driven Impacts of Absorbing Aerosols on the East Asian Summertime
 751 Climate, *J. Climate*, 30, 8929-49, <https://doi.org/10.1175/JCLI-D-16-0860.1>, 2017.
- 752 Ramanathan, V. and Carmichael, G.: Global and regional climate changes due to black
 753 carbon, *Nat. Geosci.*, 1, 221-227, <https://doi.org/10.1038/ngeo156>, 2008.
- 754 Recchia, L. G. and Lucarini, V.: Modelling the effect of aerosol and greenhouse gas
 755 forcing on the South Asian and East Asian monsoons with an intermediate-
 756 complexity climate model, *Earth Syst. Dynam.*, 14, 697-722, 10.5194/esd-14-697-
 757 2023, 2023.
- 758 Richardson, T. B., Forster, P. M., Andrews, T. and Parker, D.: Understanding the rapid
 759 precipitation response to CO₂ and aerosol forcing on a regional scale. *J. Climate*,
 760 29, 583-594, <https://doi.org/10.1175/JCLI-D-15-0174.1>, 2016.
- 761 Samset, B. H., Lund, M. T., Bollasina, M., Myhre, G. and Wilcox, L.: Emerging Asian
 762 aerosol patterns, *Nat. Geosci.*, 12, 582-584, [https://doi.org/10.1038/s41561-019-](https://doi.org/10.1038/s41561-019-0424-5)
 763 0424-5, 2019.
- 764 Sperber, K. R., Annamalai, H., Kang, I. S., Kitoh, A., Moise, A., Turner, A., Wang, B.
 765 and Zhou, T.: The Asian summer monsoon: an intercomparison of CMIP5 vs.
 766 CMIP3 simulations of the late 20th century, *Clim. Dynam.*, 41, 2711-2744,
 767 10.1007/s00382-012-1607-6, 2013.
- 768 Stjern, C. W., Samset, B. H., Myhre, G., Forster, P. M., Hodnebrog, Ø, Andrews, T.,
 769 Boucher, O., Faluvegi, G., Iversen, T., Kasoar, M., Kharin, V., Kirkevåg, A.,
 770 Lamarque, J.-F., Olivieì, D., Richardson, T., Shawki, D., Shindell, D., Smith, C.,
 771 Takemura, T. and Voulgarakis, A.: Rapid adjustments cause weak surface
 772 temperature response to increased black carbon concentrations, *J. Geophys. Res.-*
 773 *Atmos.*, 122, 11462-1481, <https://doi.org/10.1002/2017JD027326>, 2017.
- 774 Stjern, C., Joshi, M., Wilcox, L., Gollo, A. and Samset, B.: Systematic Regional Aerosol
 775 Perturbations (SyRAP) in Asia using the intermediate-resolution global climate



- 776 model FORTE2, J. Adv. Mod. Earth System, accepted, 2024.
- 777 Tian, F., Dong, B., Robson, J. and Sutton, R.: Forced decadal changes in the East Asian
- 778 summer monsoon: the roles of greenhouse gases and anthropogenic aerosols, Clim.
- 779 Dynam., <https://doi.org/10.1007/s00382-018-4105-7>, 2018.
- 780 Wang, H.: The weakening of the Asian monsoon circulation after the end of 1970's, Adv.
- 781 Atmo. Sci., 18, 376-386, <https://doi.org/10.1007/BF02919316>, 2001.
- 782 Wang, Z., Lin, L., Yang, M., Xu, Y. and Li, J.: Disentangling fast and slow responses of
- 783 the East Asian summer monsoon to reflecting and absorbing aerosol forcings,
- 784 Atmos. Chem. Phys., 17, 11075-11088, [https://doi.org/10.5194/acp-17-11075-](https://doi.org/10.5194/acp-17-11075-2017)
- 785 2017, 2017.
- 786 Webb, D. J.: An ocean model code for array processor computers, Comput. Geosci., 22,
- 787 569-578, 1996.
- 788 Westervelt, D. M., Conley, A. J., Fiore, A. M., Lamarque, J.-F., Shindell, D. T., Previdi,
- 789 M., Mascioli, N. R., Faluvegi, G., Correa, G., and Horowitz, L. W.: Connecting
- 790 regional aerosol emissions reductions to local and remote precipitation responses,
- 791 Atmos. Chem. Phys., 18, 12461-12475, [https://doi.org/10.5194/acp-18-12461-](https://doi.org/10.5194/acp-18-12461-2018)
- 792 2018, 2018.
- 793 Westervelt, D. M., You, Y., Li, X., Ting, M., Lee, D. and Ming, Y.: Relative importance
- 794 of greenhouse gases, sulfate, organic carbon, and black carbon aerosol for South
- 795 Asian monsoon rainfall changes, Geophys. Res. Lett., 47, e2020GL088363,
- 796 <https://doi.org/10.1029/2020GL088363>, 2020.
- 797 Wilcox, L. J., Dong, B., Sutton, R. T., Highwood, E. J.: The 2014 Hot, Dry Summer in
- 798 Northeast Asia, Bull. Amer. Meteor. Soc., 96, 105-110,
- 799 <https://doi.org/10.1175/BAMS-D-15-00123.1>, 2015.
- 800 Wilcox, L. J., Liu, Z., Samset, B. H., Hawkins, E., Lund, M. T., Nordling, K., Undorf,
- 801 S., Bollasina, M., Ekman, A. M. L., Krishnan, S., Merikanto, J., and Turner, A. G.: Accelerated increases in global and Asian summer monsoon precipitation from
- 802 future aerosol reductions, Atmos. Chem. Phys., 20, 11955–11977,
- 803 <https://doi.org/10.5194/acp-20-11955-2020>, 2020.
- 804 Xiang, B., Xie, S. P., Kang, S. M., and Kramer, R.: An emerging Asian aerosol dipole
- 805



806 pattern reshapes the Asian summer monsoon and exacerbates northern hemisphere
 807 warming, *npj Clim. Atmos. Sci.*, 6, 77, [https://doi.org/10.1038/s41612-023-](https://doi.org/10.1038/s41612-023-00400-8)
 808 00400-8, 2023.

809 Xie, X., Myhre, G., Liu, X., Li, X., Shi, Z., Wang, H., Kirkevåg, A., Lamarque, J. F.,
 810 Shindell, D., Takemura, T., and Liu, Y.: Distinct responses of Asian summer
 811 monsoon to black carbon aerosols and greenhouse gases, *Atmos. Chem. Phys.*, 20,
 812 11823-11839, <https://doi.org/10.5194/acp-20-11823-2020>, 2020.

813 Yang, J., Kang, S., Chen, D., Zhao, L., Ji, Z., Duan, K., Deng, H., Tripathi, L., Du, W.,
 814 Rai, M., Yan, F., Li, Y. and Gillies, R.: South Asian black carbon is threatening the
 815 water sustainability of the Asian Water Tower, *Nat. Commun.*, 13, 7360,
 816 <https://doi.org/10.1038/s41467-022-35128-1>, 2022.

817 Zhang, H., Wang, Z., Guo, P., and Wang, Z.: A modeling study of the effects of direct
 818 radiative forcing due to carbonaceous aerosol on the climate in East Asia, *Adv.*
 819 *Atmos. Sci.*, 26, 57-66, <https://doi.org/10.1007/s00376-009-0057-5>, 2009.

820 Zhong, W. Y. and Haigh, J. D.: Improved broad-band emissivity parameterization for
 821 water vapor cooling calculations, *J. Atmos. Sci.*, 52, 124-148, 1995.

822

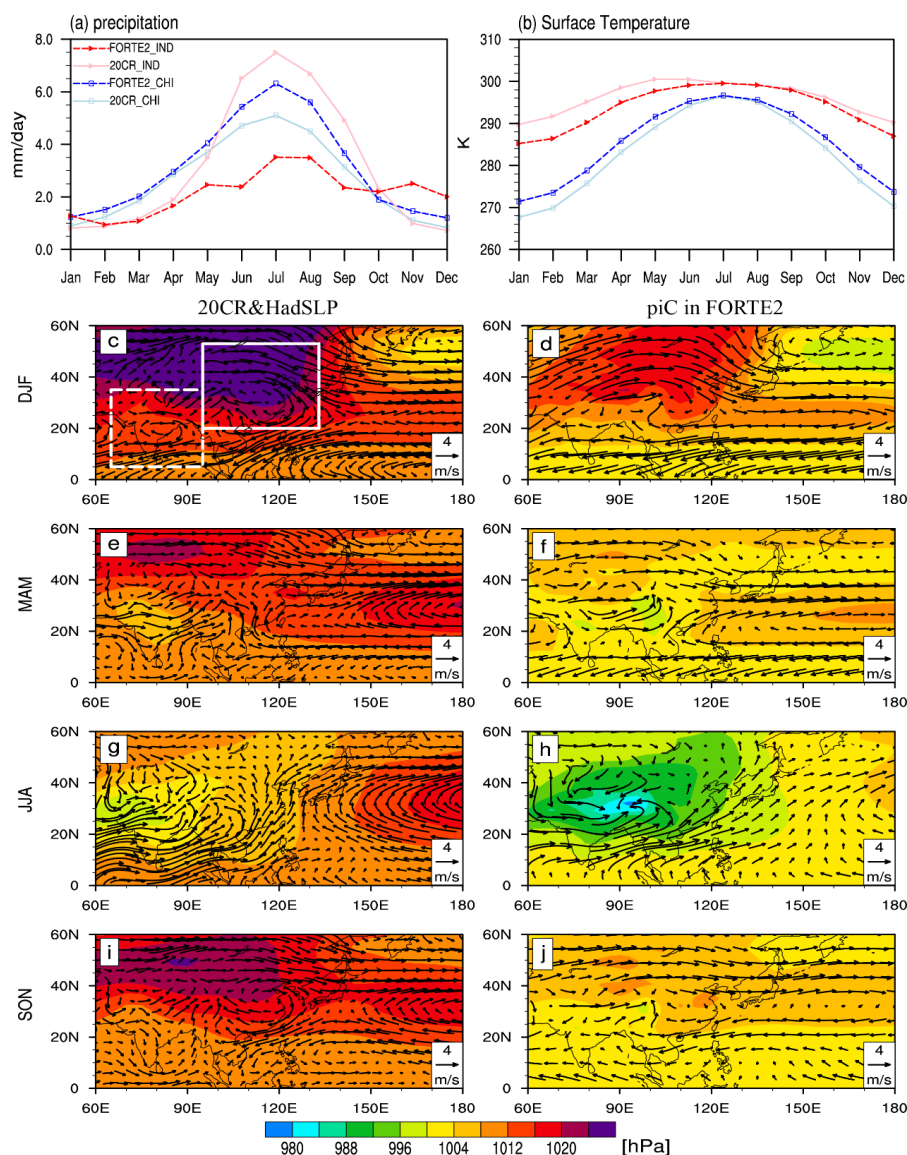


823 **Table 1.** Summary of SyRAP-FORTE2 simulations used in the study

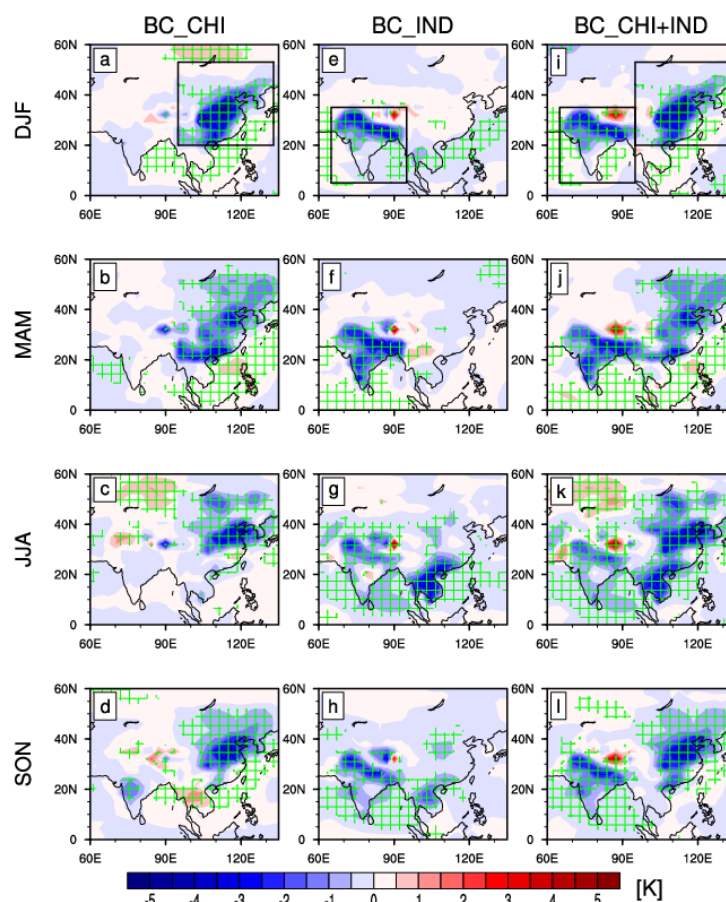
Experiment ^a	Name	Aerosol	Region	GHG	Years
Baseline	piC	No aerosol	--		
Perturbation	BC_CHI	Added BC ^b	East China (95-133°E, 20-53°N)	Preindustrial climate conditions (280 ppmv)	200
	BC_IND		India (65-95°E, 5-35°N)		
	BC_CHI+IND		both East China and India region		

824 a. only ARI effect is considered

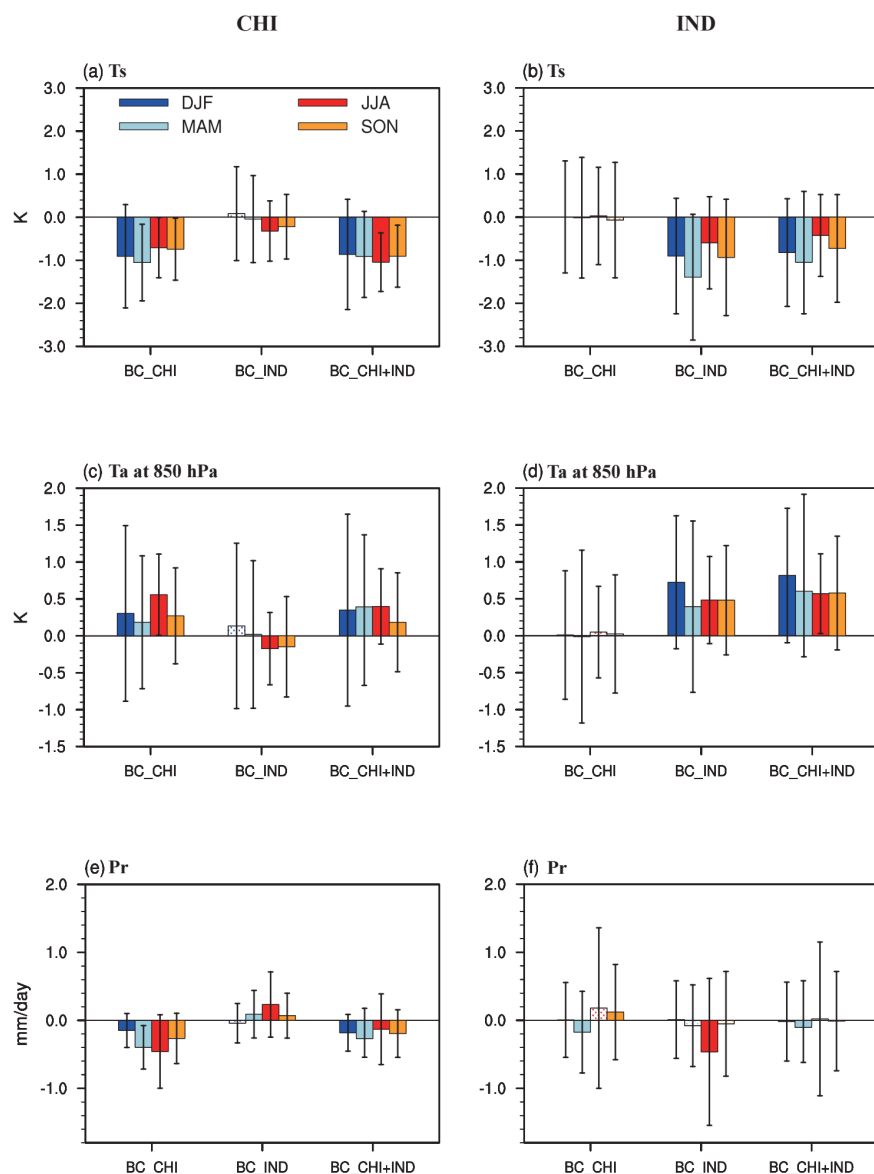
825 b. CAMSRA monthly climatology of BC AOD for 2003-2021



826
 827 **Figure 1.** Seasonal evolutions of (a) the regional mean precipitation (unit: mm/day) of
 828 20CR (solid lines) and the baseline simulation of FORTE2 (dashed lines) for East Asia
 829 (95°E-133°E, 20°N-53°N, the solid, white box in (c)) (light blue and blue lines), and
 830 India (65°E-95°E, 5°N-35°N, the dashed, white box in (c)) (pink and red lines). (b)
 831 same as (a), but for surface temperature (unit: K). Climate state of SLP (unit: hPa) and
 832 850 hPa horizontal winds (unit: m/s) in (left) 20CR and HadSLP and (right) the baseline
 833 simulation of FORTE2 in four seasons (c-j).

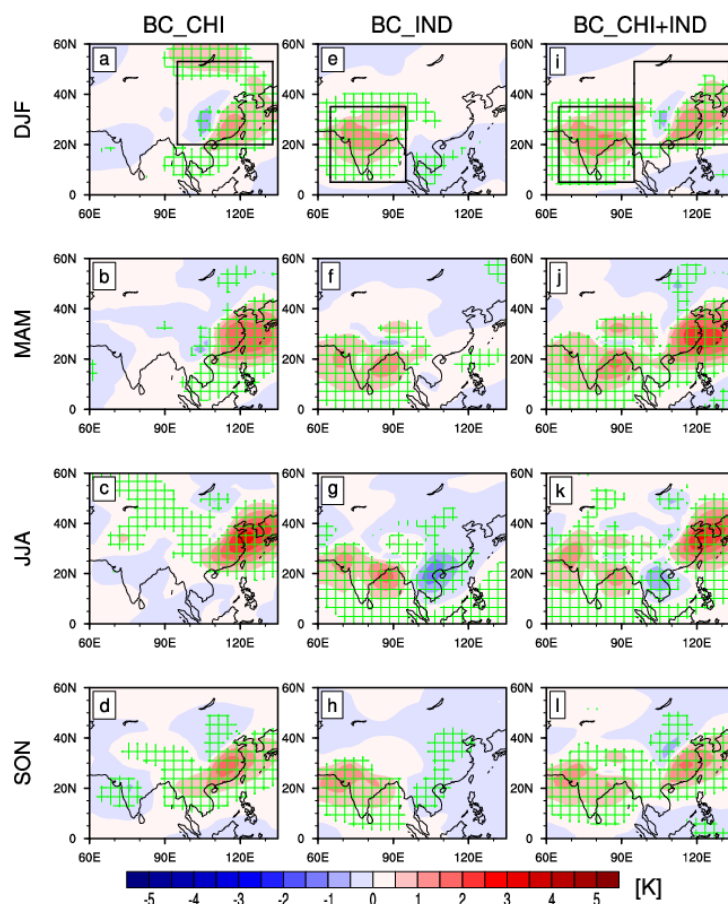


834
 835 **Figure 2.** Spatial patterns of Ts responses in (a-d) BC_CHI, (e-h) BC_IND, and (i-l)
 836 BC_CHI+IND for four seasons. The green gridlines indicate the regions where the
 837 responses are statistically significant above 95% level based on a two-tailed Student's
 838 t-test. The black boxes in (a), (e) and (i) highlight the region where BC aerosols are
 839 perturbed. Unit: K

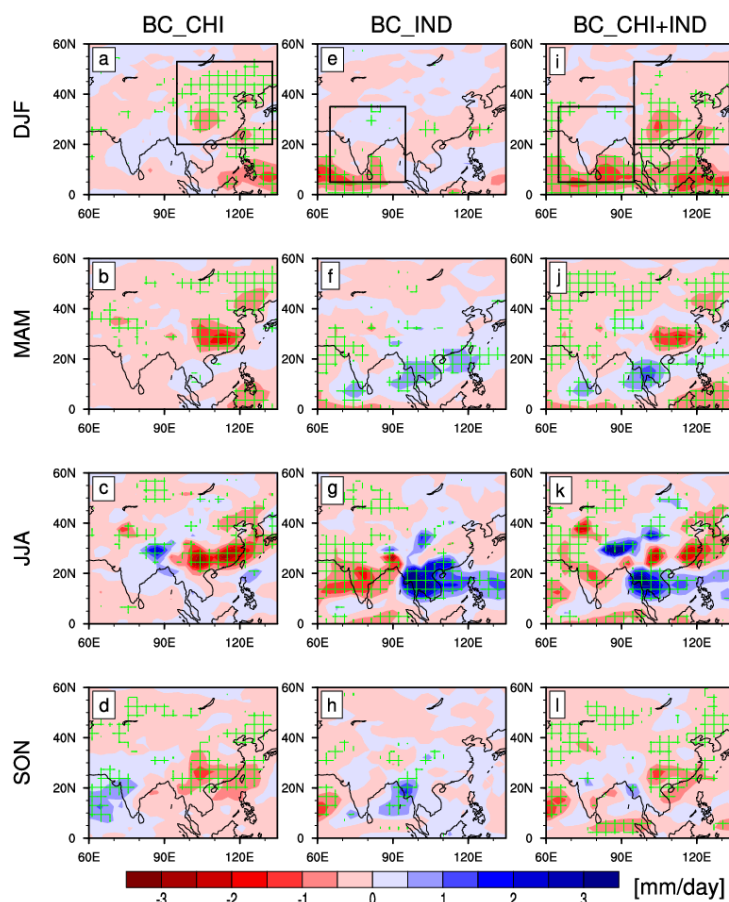


840

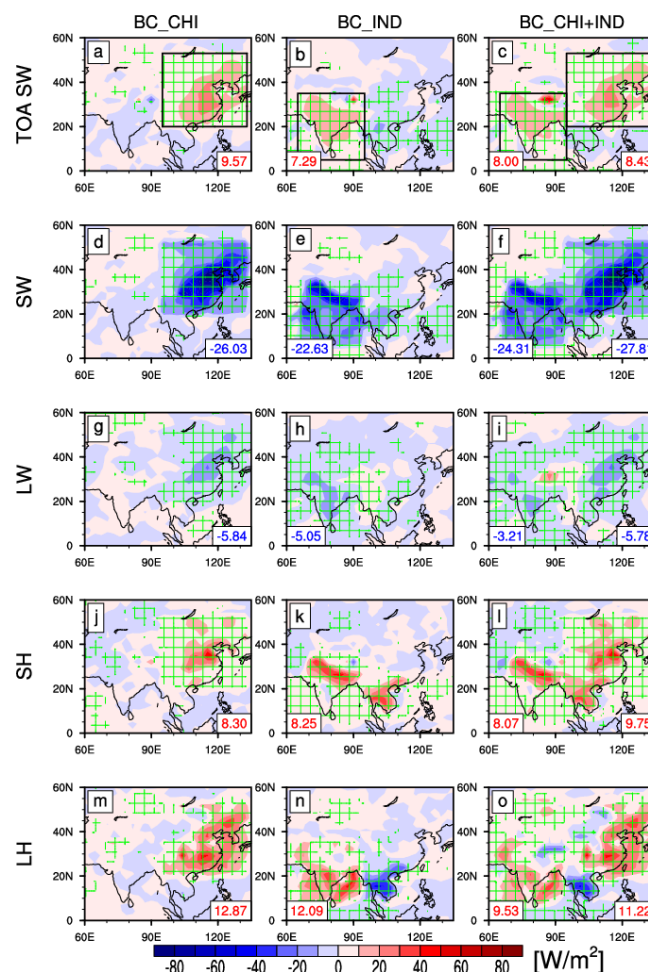
841 **Figure 3.** Area-averaged land responses of (a-b) Ts, (c-d) Ta at 850 hPa, and (e-f)
 842 precipitation over East China (CHI: 95°E-133°E, 20°N-53°N) and India (IND: 65°E-
 843 95°E, 5°N-35°N) for four seasons (DJF: blue bars, MAM: light blue bars, JJA: red bars,
 844 and SON: yellow bars). Solid bars indicate the responses are statistically significant
 845 above 95% level based on a two-tailed Student's t-test. Error bars represent ±1 standard
 846 deviations of the response.



847
848 **Figure 4.** Spatial patterns of Ta responses at 850 hPa in (a-d) BC_CHI, (e-h) BC_IND,
849 and (i-l) BC_CHI+IND for four seasons. The green gridlines indicate the regions where
850 the responses are statistically significant above 95% level based on a two-tailed
851 Student's t-test. The black boxes in (a), (e) and (i) highlight the region where BC
852 aerosols are perturbed. Unit: K

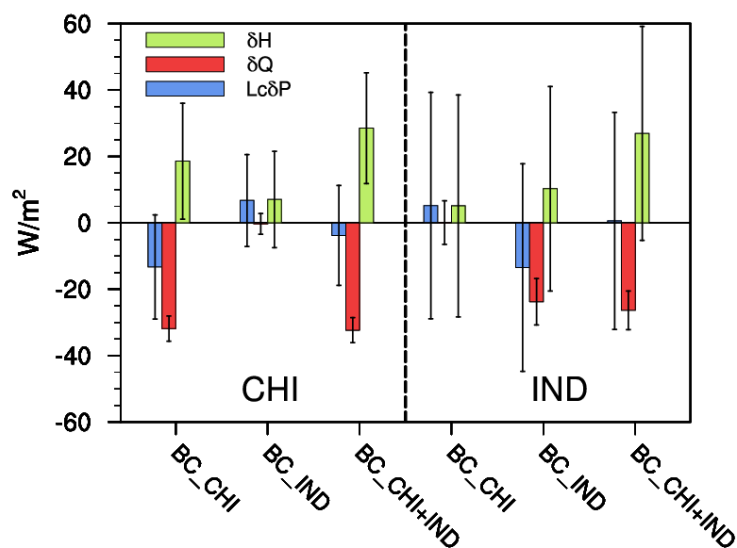


853
 854 **Figure 5.** Spatial patterns of precipitation responses in (a-d) BC_CHI, (e-h) BC_IND,
 855 and (i-l) BC_CHI+IND for four seasons. The green gridlines indicate the regions where
 856 the responses are statistically significant above 95% level based on a two-tailed
 857 Student's t-test. The black boxes in (a), (e) and (i) highlight the region where BC
 858 aerosols are perturbed. Unit: mm/day
 859



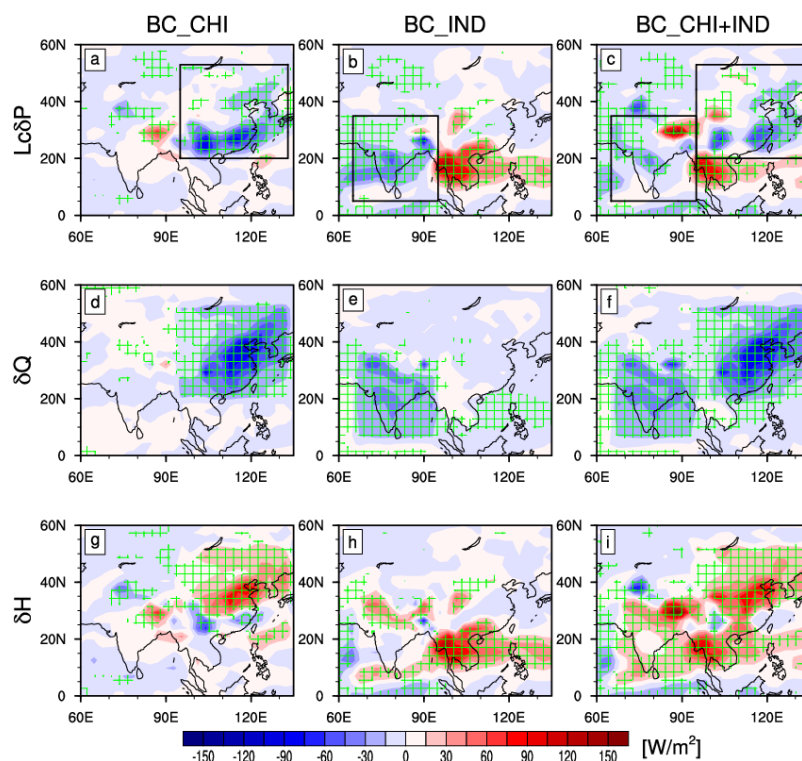
860

861 **Figure 6.** Spatial patterns of net TOA and surface energy responses in summer in
 862 BC_CHI, BC_IND, and BC_CHI+IND, respectively. (a-c) TOA SW, (d-f) surface SW,
 863 (g-i) surface LW, (j-l) surface SH, and (m-o) surface LH. Positive values mean
 864 downward for radiation and flux changes. Area-averaged values over East China and
 865 India are given in the lower right corners and lower left corners, respectively. The green
 866 gridlines indicate the regions where the responses are statistically significant above 95%
 867 level based on a two-tailed Student's t-test. The black squares highlight the regions
 868 where BC are perturbed. Units: W/m^2



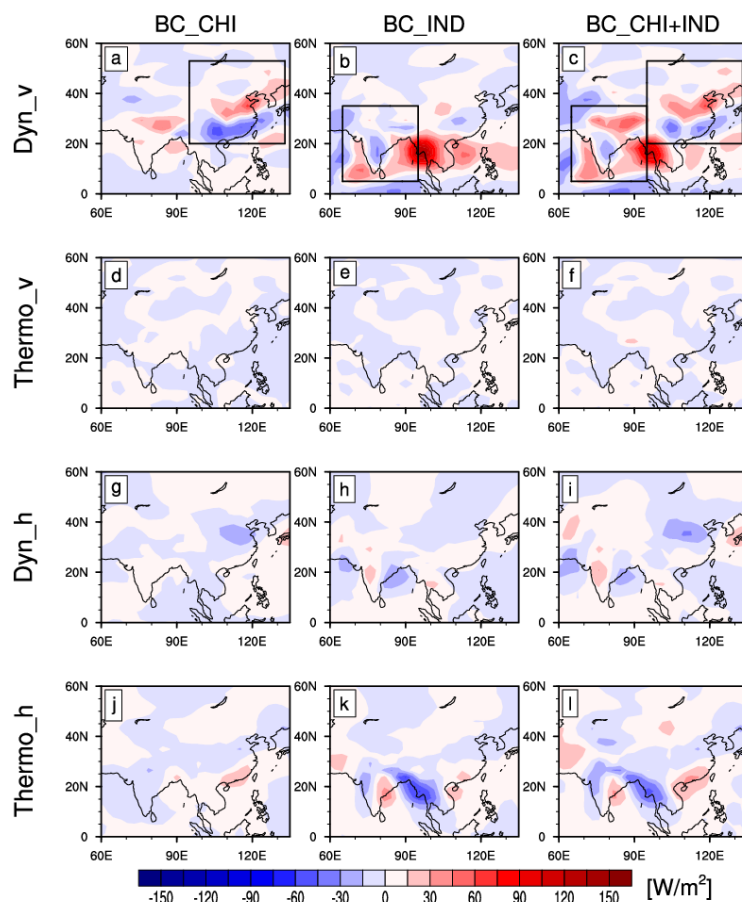
869

870 **Figure 7.** Summer area-averaged responses of the atmospheric energy budget terms
 871 over East China (CHI: 95°E-133°E, 20°N-53°N) and India (IND: 65°E-95°E, 5°N-
 872 35°N) in BC_CHI, BC_IND, and BC_CHI+IND. Error bars represent ± 1 standard
 873 deviations of the response. Unit: W/m^2



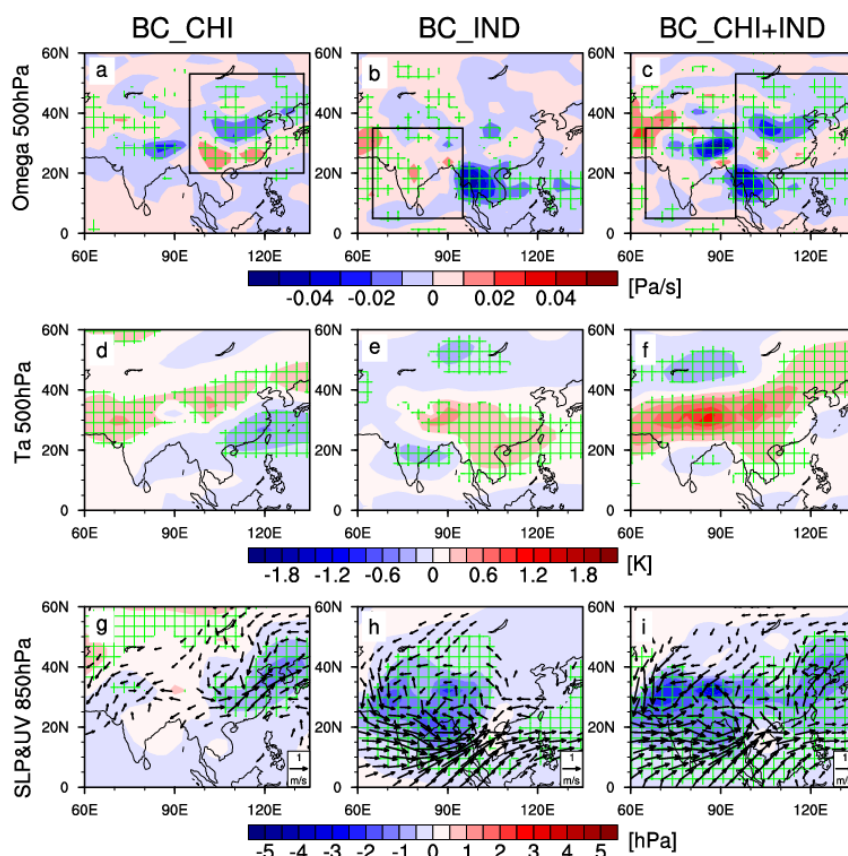
874

875 **Figure 8.** Summer spatial patterns of responses of the atmospheric energy budget terms
 876 in BC_CHI, BC_IND, and BC_CHI+IND. (a-c) $L_c\delta P$, (d-f) δQ and (g-i) δH . The green
 877 gridlines indicate the regions where the responses are statistically significant above 95%
 878 level based on a two-tailed Student's t-test. The black squares highlight the regions
 879 where BC are perturbed. Unit: W/m^2

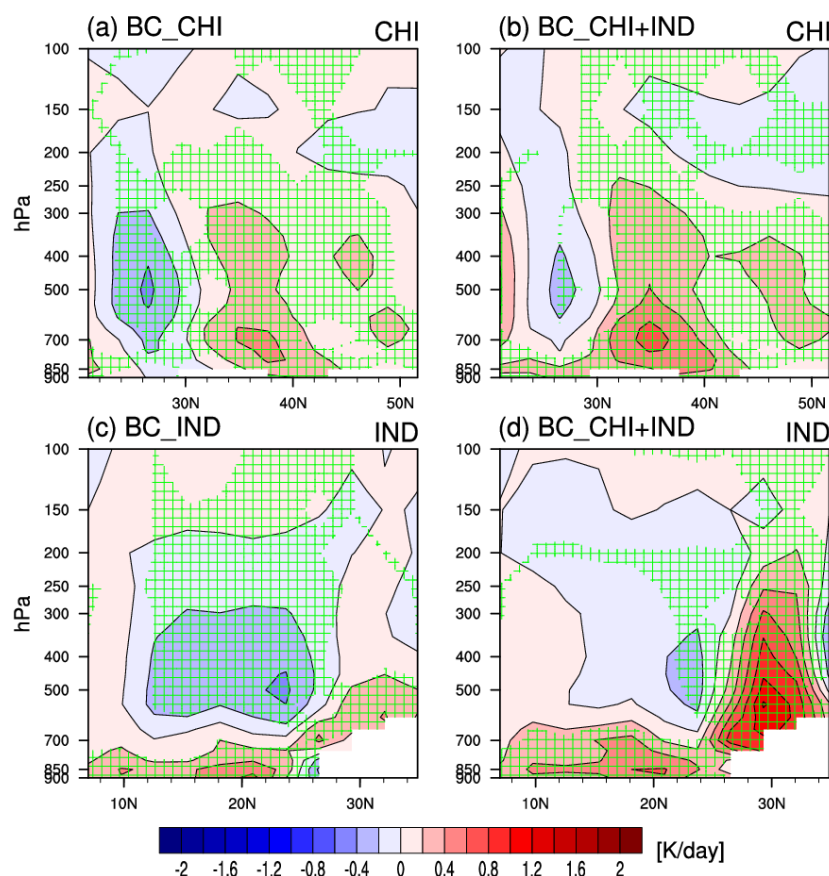


880

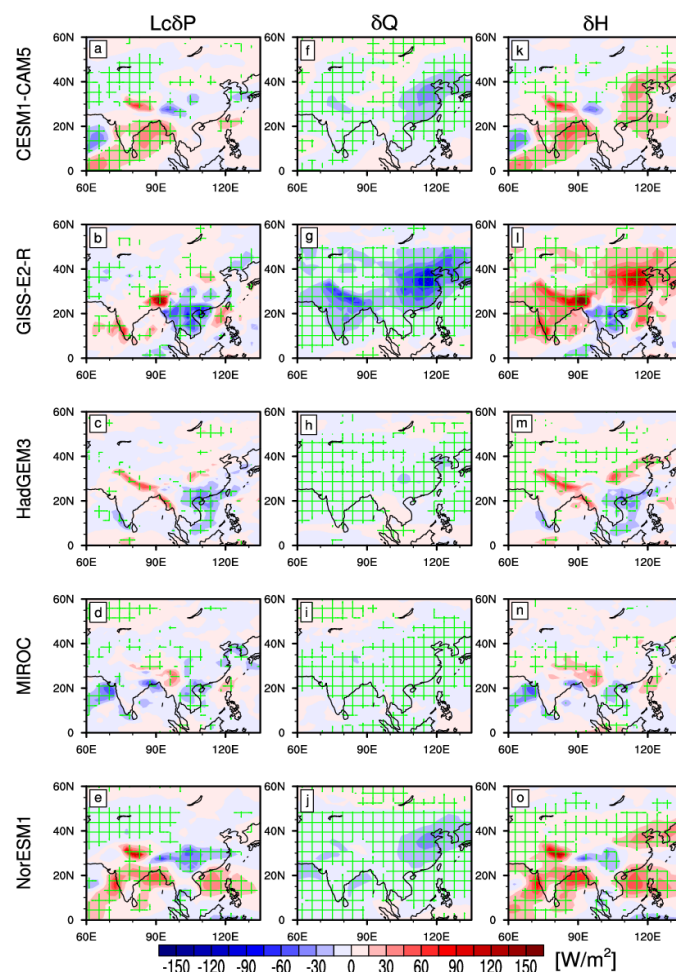
881 **Figure 9.** Summer spatial patterns of responses in the four terms decomposed by ΔH_m
 882 in BC_CHI, BC_IND, and BC_CHI+IND. (a-c) the dynamic components with changes
 883 in vertical atmospheric circulations (ΔH_{Dyn_v}), (d-f) the thermodynamic components
 884 with changes in vertical atmospheric circulations ($\Delta H_{\text{Thermo}_v}$), (g-i) dynamic
 885 components with changes in horizontal DSE gradients (ΔH_{Dyn_h}), and (j-l)
 886 thermodynamic components with changes in horizontal DSE gradients ($\Delta H_{\text{Thermo}_h}$)
 887 The black squares highlight the regions where BC are perturbed. Unit: W/m^2
 888



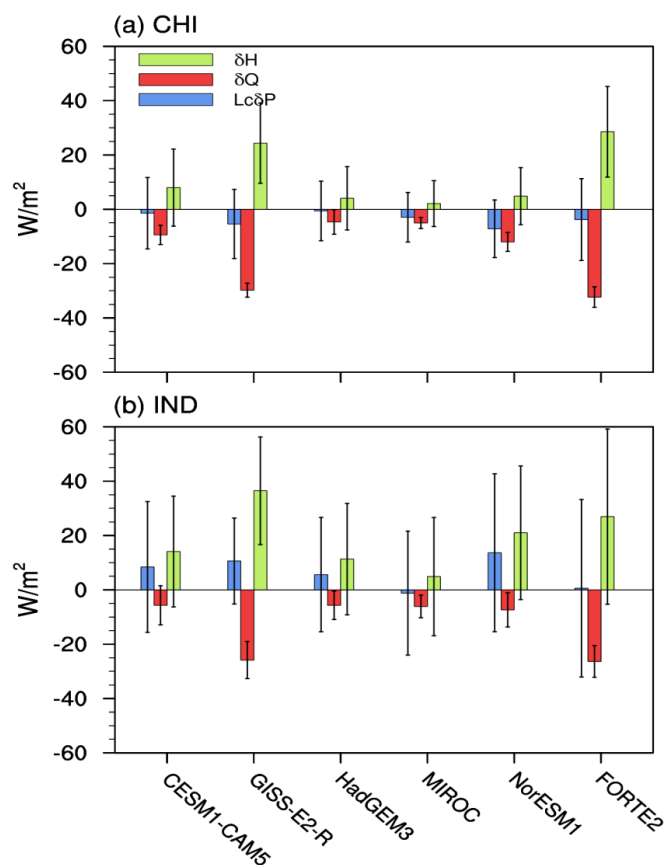
889
 890 **Figure 10.** Summer spatial patterns of responses in (a-c) Omega at 500 hPa (Unit: Pa/s),
 891 (d-f) Ta at 500 hPa (Unit: K), and (g-i) SLP (Unit: hPa) and horizontal wind at 850 hPa
 892 (Unit: m/s) in BC_CHI, BC_IND and BC_CHI+IND. The green gridlines indicate the
 893 regions where the responses are statistically significant above 95% level based on a
 894 two-tailed Student's t-test. Wind vectors are only shown for grid boxes where at least
 895 one component of the wind significant above the 95% level are shown. The black
 896 squares highlight the regions where BC are perturbed.



897
 898 **Figure 11.** Zonal mean of diabatic heating responses averaged over (a-b) East China
 899 (95°E-133°E, the black square in Fig.10a) for BC_CHI and BC_CHI+IND, and over
 900 (c-d) India (65°E-95°E, the black square in Fig.10b) for BC_IND and BC_CHI+IND
 901 in summer. The green gridlines indicate the regions where the responses are statistically
 902 significant above 95% level based on a two-tailed Student's t-test. The white part
 903 indicates a symbol of topography. Unit: K/day



904
 905 **Figure 12.** Summer spatial patterns of responses of the atmospheric energy budget
 906 terms in the five PDRMIP models. (a-e) $L_c\delta P$, (f-j) δQ and (k-o) δH . The green
 907 gridlines indicate the regions where the responses are statistically significant above 95%
 908 level based on a two-tailed Student's t-test. Unit: W/m^2



909

910 **Figure 13.** Summer area-averaged responses of the atmospheric energy budget terms
 911 over (a) East China (CHI: 95°E-133°E, 20°N-53°N) and (b) India (IND: 65°E-95°E,
 912 5°N-35°N) in the five PDRMIP models and the BC_CHI+IND simulation in FORTE2.
 913 Error bars represent ± 1 standard deviations of the response. Unit: W/m^2